Dalton Transactions

Origin of the 29Si NMR Chemical Shift in R3Si–X and Relationship to the formation of Silylium (R3Si+) Ions

Journal:	*Dalton Transactions*
Manuscript ID	DT-ART-06-2020-002099.R2
Article Type:	Paper
Date Submitted by the Author:	30-Jul-2020
Complete List of Authors:	Huynh, Winn; University of California Conley, Matthew; University of California,

Origin of the ^{29}Si NMR Chemical Shift in $R_3Si–X$ and Relationship to the formation of Silylium (R_3Si^+) Ions

Winn Huynh and Matthew P. Conley*

Department of Chemistry, University of California, Riverside, California 92507, United States

ABSTRACT: The origin in deshielding of ^{29}Si NMR chemical shifts in $R_3Si–X$, where X = H, OMe, Cl, OTf, $[CH_6B_{11}X_6]$, toluene, and O_X (O_X = surface oxygen), as well as $^{i}Pr_3Si^+$ and Mes_3Si^+ were studied using DFT methods. At the M06-L/6-31G(d,p) level of theory the geometry optimized structures agree well with those obtained experimentally when available. The trends in ^{29}Si NMR chemical shift also reproduce experimental trends; $^{i}Pr_3Si–H$ has the most shielded ^{29}Si NMR chemical shift and free $^{i}Pr_3Si^+$ or isolable Mes_3Si^+ have the most deshielded ^{29}Si NMR chemical shift. Natural localized molecular orbital (NLMO) analysis of the contributions to paramagnetic shielding (σ^p) in these compounds shows that Si–R (R = alkyl, H) bonding orbitals are the major contributors to deshielding in this series. The Si–R bonding orbitals are coupled to the empty p-orbital in $^{i}Pr_3Si^+$ or Mes_3Si^+, or to the $\sigma^*_{Si–X}$ orbital in $R_3Si–X$. This trend also applies to surface bound $R_3Si–O_X$. This model also explains chemical shift trends in recently isolated $^{t}Bu_2SiH_2^+$, $^{t}BuSiH_2^+$, and SiH_3^+ that show more shielded ^{29}Si NMR signals than R_3Si^+ species. There is no correlation between isotropic ^{29}Si NMR chemical shift and charge at silicon.

Introduction

The silicon derivatives of carbocations (R_3C^+) are silylium ions (R_3Si^+). R_3C^+ species are accessible in liquid superacidic media containing weakly coordinating anions (e.g. $Sb_2F_{11}^-$) and contain sp^2 hybridized planar structures at the central carbon atom.[1] Synthesis of R_3Si^+ required counter anions with higher stability and lower nucleophilicity than those needed to isolate R_3C^+.[2] These studies showed that R_3Si^+ containing weakly coordinating $B(C_6F_5)_4^-$ or $[CH_6B_{11}Br_6]$ anions were isolable as crystalline solids, though with several distinguishing structural features that contrast R_3Si^+ from R_3C^+. For example, the silylium fragment in $[^{i}Pr_3Si][CH_6B_{11}Br_6]$ contains average C–Si–C bond angles of 117°, a significant deviation from planarity expected for an sp^2 hybridized silicon.[3] Further ambiguities arose from the ability of R_3Si^+ to interact with very weak nucleophiles, such as toluene in $[Et_3Si(toluene)][B(C_6F_5)_4]$,[4] that distort silicon from planarity and delocalize charge into the aromatic ring. The controversy surrounding the isolation of silylium cations[5] was not settled until Reed and Lambert isolated the $[Mes_3Si][CH(Me_5)B_{11}Br_6]$ salt that contains a planar sp^2 hybridized silicon.[6]

During these investigations, which largely focused on X-ray diffraction analyses, the ^{29}Si NMR chemical shift was recognized as a diagnostic indicator for silylium character in R_3Si^+ salts that deviated from planarity.[7] Figure 1 summarizes reported ^{29}Si NMR chemical shift for selected $R_3Si–X$ and $[R_3Si][X]$ ion-pairs. The general trend shown in Figure 1 is that as charge accumulates at silicon the ^{29}Si NMR chemical shift value increases. This trend is particularly clear for $^{i}Pr_3Si–X$. The ^{29}Si NMR chemical shift of $^{i}Pr_3Si–H$ in toluene-d_8 is 12 ppm. Replacing the Si–H group with electron withdrawing groups results in a downfield shift of the ^{29}Si NMR signal, maximizing at the $[^{i}Pr_3Si][CH_6B_{11}Cl_6]$ salt that has a ^{29}Si NMR chemical shift of 115 ppm in the solid-state. This trend was supported by DFT calculations of $Me_3Si–Cl$ as a function of Si–Cl bond distance. As the Si–Cl bond length increases positive charge accumulates at silicon and ^{29}Si NMR signals are predicted at higher chemical shift values.[7] The conclusions from this study that charge at silicon relates to ^{29}Si NMR chemical shift is a metric that has been widely used to quantify silylium character in R_3Si^+ as isolable molecular salts,[8] and recently to descriptions of R_3Si^+ supported on oxide surfaces.[9]

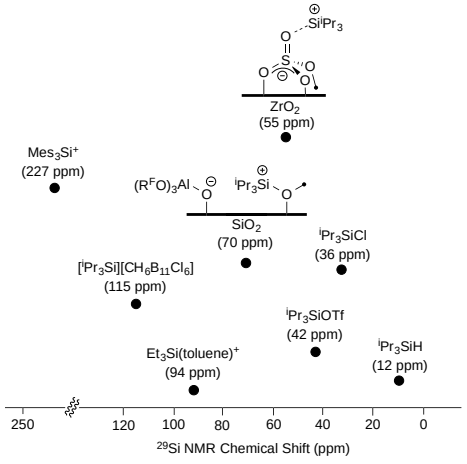

Figure 1. Selected ^{29}Si NMR chemical shifts for $R_3Si–X$.

Magnetic shielding of an NMR active nucleus as a result of being placed in a strong external magnetic field ($\mathbf{B}_0$) is described by the three principal components of the second rank

tensor (σ_{11}, σ_{22}, σ_{33}) shown in eq 1. The most deshielded component is σ_{11}, and the most shielded component is σ_{33}. The values of (σ_{11}, σ_{22}, σ_{33}) average to isotropic shielding values in solution due to rapid tumbling such that $\sigma_{iso} = 1/3(\sigma_{11} + \sigma_{22} + \sigma_{33})$. Calibration of σ_{iso} to a reference compound, such as Me_4Si for ^{29}Si NMR spectra, using eq 2 results in the more familiar chemical shift (δ).

$$\sigma_{iso} = \begin{matrix} \sigma_{11} & 0 & 0 \\ 0 & \sigma_{22} & 0 \\ 0 & 0 & \sigma_{33} \end{matrix} \quad (1)$$

$$\delta = \frac{\sigma_{ref} - \sigma_{iso}}{1 - \sigma_{ref}} \quad (2)$$

Shielding is related to the effect of $\mathbf{B}_0$ on the flow of electrons around the NMR active nucleus that induces a small magnetic field opposing $\mathbf{B}_0$, usually referred to as $\mathbf{B}_i$. Ramsey decomposed shielding contributions into diamagnetic shielding (σ^d) and paramagnetic shielding (σ^p), eq 3.

$$\sigma_{iso} = \sigma^d + \sigma^p \quad (3)$$

Chemical environment does not appreciably affect σ^d for heavy atoms (i.e. ^{13}C, ^{19}F, ^{29}Si, ^{31}P, etc.), but rather σ^p determines chemical shift trends. This behavior is related to anisotropies introduced by accessible p-orbitals that form σ- and π-bonds in these elements. Unlike σ^d, which is a consequence of the effect of $\mathbf{B_0}$ on the ground-state wavefunction, σ^p couples the ground state wavefunction (ϕ_0) to an excited state wavefunction (ϕ_n) through the angular momentum operator ($\hat{L}_{ki}$, where *ki* = element of the shielding tensor, eq 4). The denominator in eq 4 indicates that if ϕ_0 and ϕ_n are close in energy a large σ^p contribution is expected. This situation is maximized when ϕ_0 is the highest occupied molecular orbital (HOMO) and ϕ_n is the lowest unoccupied molecular orbital (LUMO). Orbitals close to the HOMO and LUMO also can result in large σ^p.[10]

$$\sigma_{ij}^{p} \propto \frac{\langle \varphi_0 | \hat{L}_{ki} | \varphi_n \rangle \left\langle \varphi_n \left| \frac{\hat{L}_{kNj}}{r_{kN}^3} \right| \varphi_0 \right\rangle}{\Delta E_{n-0}} \quad (4)$$

Orbital rotation models are useful to visualize these effects, which is shown for a *N*-heterocyclic silylene in Figure 2. The ^{29}Si NMR chemical shifts of *N*-heterocyclic silylenes are deshielded, ranging from ~75 – 120 ppm. The origin of this deshielding is related to the orientation of the σ_{11} component for the shielding tensor, which was measured experimentally using solid-state NMR spectroscopy and verified using DFT methods, Figure 2.[11] These data show that the shielding tensor orients σ_{11} in the N–Si–N plane perpendicular to the filled silylene lone pair orbital, the HOMO in a *N*-heterocyclic silylene. Rotation of this orbital by 90° ($\hat{L}_{11}$) results in ψ_n, which is the empty p-orbital that is the LUMO in a *N*-heterocyclic silylene. This orientation maximizes σ^p deshielding, and results in the downfield chemical shift values observed for the silylene silicon. Similar deshielding trends properties also apply to $R_2Si{=}SiR_2$,[12] $RSi{\equiv}SiR$,[13] $R_2Si{=}CR'_2$,[14] $R_2Si{=}X$ (X = O, S),[15] and heteroatom substituted silyl lithiums.[16]

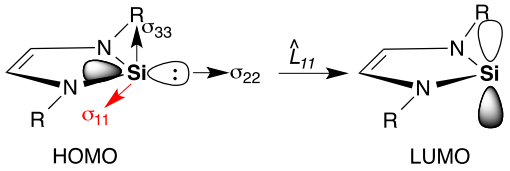

Figure 2. Orientation of the shielding tensor in a *N*-heterocyclic silylene, and coupling of the HOMO to the LUMO through the angular momentum operator $\hat{L}_{11}$.

Orbital rotation models are widely applicable and relate NMR chemical shifts to electronic structures in organic molecules,[17] aryllithium reagents,[18] and organometallic complexes.[19] Based on these arguments, the origin of the ^{29}Si NMR chemical shift trends shown in Figure 1 are probably not directly related to charge at silicon, but rather the magnitude of σ^p. This study describes the origin of deshielding of ^{29}Si NMR chemical shifts in $R_3Si{-}X$ using DFT methods. The chemical shift trend shown in Figure 1 is dominated by contributions from σ^p, which is maximized when occupied Si–C bonding orbitals are perpendicular to the empty p-orbital on silicon, which occurs for free silylium ions. There is no relationship between charge at silicon and ^{29}Si NMR chemical shift.[20]

Computational Methods

The geometries of all structures were optimized in Gaussian 09[21] using the M06-L functional[22] at the 6-31G** level of theory for H, B, C, O, Si and Cl. Heavier elements (Zr, Br, I) were described with the SDD basis set. Frequency calculations at this level of theory produced no imaginary frequencies, indicating a ground-state energy minimized structure. **1** – **3** were calculated as free cations, **4** – **8** were calculated as neutral ion-pairs, **9** was calculated as the anion, and **10** – **13** were calculated as molecular species.

The NMR parameters are calculated the Amsterdam Density Functional (ADF) suite,[23] using the GIAO method[24] with the PBE functional, the TZ2P basis set on silicon and zirconium, and the DZ basis set on all other atoms. NMR calculations with the meta-GGA functional M06-L is not yet supported in ADF. However, the combination of geometry optimization in G09 at the M06-L/6-31G**/SDD level of theory, followed by computation of NMR parameters in ADF at the PBE/TZ2P(Si, Zr)/DZ results in good agreement with experiment (Table S1). Natural Localized Molecular Orbital (NLMO)[25] contributions to shielding were also calculated at this level of theory, with scalar relativistic ZORA included in this analysis.[26] This analysis in ADF gives shielding (σ) as the sum of diamagnetic shielding (σ^d) and of the full paramagnetic shielding term (σ^{p+so}), which is the sum of paramagnetic shielding and spin-orbit contributions. In this study the spin-orbit contributions are negligible. Therefore, we refer to paramagnetic shielding as σ^p for the species studied here. The canonical orbitals for **1** and **5** were calculated at the same level of theory to extract energies for the orbitals contributing to σ^p from the NLMO analysis.

Results and Discussion

$R_3Si–X$ were studied using DFT methods based on the availability of crystallographic and ^{29}Si NMR data to calibrate the computational analysis of NMR properties given below. The geometries of these compounds were optimized at the M06-L/6-31G(d,p) level of theory, and structures of these compounds are shown in Figure 3. Calculated structures and coordinates for these compounds are given in the Supporting Information. $^{i}Pr_3Si^+$ (**1**), Mes_3Si^+ (**2**), and $Et_3Si(toluene)^+$ (**3**) were calculated without anions, while **4**-**9** were calculated as ion-pairs.

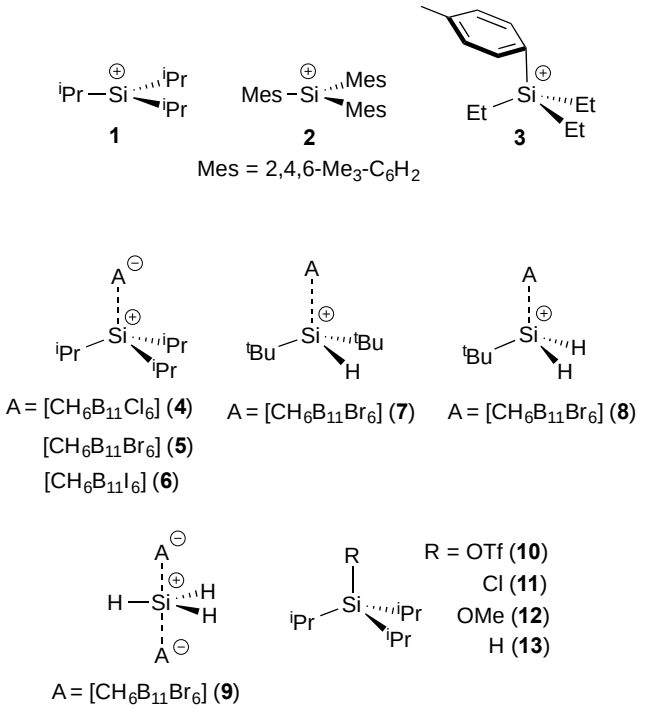

Figure 3. Structures of **1-13** optimized at the M06-L/Br, I(SDD); 6-31G** level of theory.

Key structural data of the optimized geometries of $R_3Si–X$ are summarized in Table 1, and compared to experimental data when available. This level of theory accurately reproduces Si–C and Si–H bond lengths, and captures trends in Si–X bond distances for anion containing structures, across the series of compounds in Figure 1. The Si–C or Si–H bond distances are roughly constant across the series of $R_3Si–X$, indicating that these distances are not a clear indicator of silylium character.

Table 1 shows that the $R_3Si–X$ approaches R_3Si^+ the silicon becomes more planar, which is expected for a sp^2 hybridized silylium ion. For example, the sum of C–Si–C bond angles in free $^{i}Pr_3Si^+$ (**1**) is 358.4°. This value is close to that obtained experimentally, and at this level of theory, for Mes_3Si^+ (**2**, $\Sigma_{C\text{-}Si\text{-}C}$ = 360.0°). The C–Si–C bond angles contract in silylium species coordinated to weak ligands, such as toluene in $Et_3Si(toluene)^+$ (**3**), indicating that the silicon pyramidalizes. This behavior is common, and observed in $[^{i}Pr_3Si][CH_6B_{11}Cl_6]$ (**4,** $\Sigma_{C\text{-}Si\text{-}C}$ = 348.4°) due to an interaction between silicon and one of the halides on the carborane anions ($d_{Si\text{-}Cl}$ = 2.26 Å). The $\Sigma_{C\text{-}Si\text{-}C}$ bond angles is 347.1° in $[^{i}Pr_3Si][CH_6B_{11}Br_6]$ (**5**) and 342.5° in $[^{i}Pr_3Si][CH_6B_{11}I_6]$ (**6**), indicating that these species also contain pyramidalized silicon, and reproduce trends in C–Si–C angles for these compounds observed experimentally.[7]

Table 1. Key geometric data for $R_3Si–X$.[a]

$R_3Si–X$	Average $r_{Si\text{-}R}$ (Å)	$r_{Si\text{-}X}$ (Å)	Σ(R-Si-R) (deg.)	Ref.
1	1.86	---	358.4	---
2	1.83 (1.82)	---	360.0 (360.0)	6
3	1.87 (1.85)	2.13 [2.195(11)]	342.5 (341.6)	27
4	1.88 (1.85)	2.26 [2.323(3)]	348.4 (351.9)	2a
5	1.88 (1.86)	2.45 [2.479(9)]	347.1 (350.9)	3
6	1.89 (1.88)	2.63 [2.660(7)]	342.5 (346.8)	2a
7	C: 1.89 (1.88) H: 1.48 (1.52)	2.41 [2.4110(14))	345.4 (347.9)	8d
8	C: 1.88 (1.85) H: 1.47 (1.37, 1.51)	2.37 [2.3777(16))	343.4 (342.9)	8d
9	H: 1.46 (1.50)	2.65, 2.65 [2.477(4), 2.770(4) 2.77)	360.0 (357.0)	8d
10	1.88	1.76	343.7	--
11	1.89	2.10	337.1	--
12	1.90	1.68	334.0	--
13	1.90	1.50	333.7	--
14	1.89	1.68	334.0	--
15	1.89	1.83	333.4	--
16	1.89	1.71	337.9	--
17	1.89	1.77	338.4	--

[a] – Bond distances and bond angles from $R_3Si–X$ optimized at the M06-L/Zr, Br, I(SDD); 6-31G** level of theory. Values given in parentheses are experimental values from X-ray crystal structures.

Table 1 shows that the $R_3Si–X$ approaches R_3Si^+ the silicon becomes more planar, which is expected for a sp^2 hybridized silylium ion. For example, the sum of C–Si–C bond angles in free $^{i}Pr_3Si^+$ (**1**) is 358.4°. This value is close to that obtained experimentally, and at this level of theory, for Mes_3Si^+ (**2**, $\Sigma_{C\text{-}Si\text{-}C}$ = 360.0°). The C–Si–C bond angles contract in silylium species coordinated to weak ligands, such as toluene in $Et_3Si(toluene)^+$ (**3**), indicating that the silicon pyramidalizes. This behavior is common, and observed in $[^{i}Pr_3Si][CH_6B_{11}Cl_6]$ (**4,** $\Sigma_{C\text{-}Si\text{-}C}$ = 348.4°) due to an interaction between silicon and one of the halides on the carborane anions ($d_{Si\text{-}Cl}$ = 2.26 Å). The $\Sigma_{C\text{-}Si\text{-}C}$ bond angles is 347.1° in $[^{i}Pr_3Si][CH_6B_{11}Br_6]$ (**5**) and 342.5° in $[^{i}Pr_3Si][CH_6B_{11}I_6]$ (**6**), indicating that these species also contain pyramidalized silicon, and reproduce trends in C–Si–C angles for these compounds observed experimentally.[7]

Similar behavior is observed for [^{t}Bu$_2$SiH][$CH_6B_{11}Br_6$] (**7**, $\Sigma_{C\text{-}Si\text{-}C}$ = 345.4°), and [^{t}Bu-SiH$_2$][$CH_6B_{11}Br_6$] (**8**, $\Sigma_{R\text{-}Si\text{-}R}$ = 343.4°). [SiH_3][$CH_6B_{11}Br_6$]$_2^-$ (**9**) is an exception, and contains a planar silicon ($\Sigma_{H\text{-}Si\text{-}H}$ = 360.0°). In the solid-state **9** exists as an infinite polymer of alternating SiH_3^+ and $CH_6B_{11}Br_6^-$ that enforces the trigonal bipyramidal structure at silicon, resulting in planarity in the plane defined by the three Si–H bonds.

The $\Sigma_{C\text{-}Si\text{-}C}$ bond angles in ^{i}Pr$_3$Si–OTf (**10**) is 343.7°, close to the value obtained for [^{i}Pr$_3$Si][$CH_6B_{11}X_6$] **(4-6)**. However, the Si–O bond in **10** is far shorter than the Si–X bond in a carborane salt, and is a reflection of the more weakly coordinating carborane anion relative to a triflate anion. As X becomes more coordinating to the silicon, the sum of the C–Si–C bond angles continues to decrease from 337.1° in ^{i}Pr$_3$Si–Cl (**11**), to 334.0° in ^{i}Pr$_3$Si–OMe (**12**) and to 333.7° in ^{i}Pr$_3$Si–H (**13**).

1 and **2** are "free" silylium ions, and show geometrical features expected for a planar silicon in a R_3Si^+ cation. **3** – **8** also reproduce trends in experimental data, and supports the conclusion that very weak nucleophiles, such as toluene or halogenated carborane ions, result in distortions expected for planar silylium geometries. However, **3** – **8** behave like silylium ions, and Reed referred to this class of species as "silylium-like" based on their structural and spectroscopic behaviors.[2a] As expected, a significant contraction of the C–Si–C bond angle was observed in ^{i}Pr$_3$Si–X containing groups that do not form silylium ions (**10** – **13**).

R_3Si^+ species can also form on high surface area oxides. Oxide surfaces are terminated with –OH sites, and the acidity of these sites relates to the ability of a surface oxygen to form $R_3Si–O_X$ (O_X = surface oxygen) or [R_3Si][O_X]. Partially dehydroxylated silica contains –OH sites that behave as weak acids, and react with silylating agents to form $R_3Si–O_X$. This assignment is supported by solid-state ^{29}Si NMR measurements, which contain signals near ~10 ppm.[28] Oxides containing –OH sites that behave as stronger acids than silanols on partially dehydroxylated silica, such as sulfated zirconium oxide (**SZO**) or silica contacted with Al(OC(CF$_3$)$_3$)$_3$*PhF to form very acidic –OH sites, react with allyltriisopropylsilane to form [^{i}Pr$_3$Si][O_X] based on the deshielded ^{29}Si NMR signal in these materials and their reactivity towards C–F bonds.[9]

Four cluster models to approximate ^{i}Pr$_3$Si–sites on these oxides are shown in Figure 4. An isolated silanol, which is the major surface species for silica partially dehydroxylated at 700 °C, was approximated with the –SiH_3 capped poly-oligosequisiloxane,[29] and capping the remaining silanol in this cluster with a triisopropylsilyl group results in ^{i}Pr$_3$Si–O_X (**14**), which contains a pyramidal silicon in the ^{i}Pr$_3$Si-fragment ($\Sigma_{C\text{-}Si\text{-}C}$ = 334.0°) with a Si–O bond length of 1.68 Å. Coordination of Al(OC(CF$_3$)$_3$)$_3$*PhF to the isolated silanol in this cluster reproduces spectroscopic trends observed experimentally for the acidic bridging silanol, and replacing the acidic proton with ^{i}Pr$_3$Si$^+$ forms [^{i}Pr$_3$Si][O_X] (**15**).[9b] The ^{i}Pr$_3$Si$^+$ site in **15** coordinates to the least sterically hindered Si–O–Si bridge, and does not interact with C–F bonds from the anionic $(R^FO)_3Al–OSi\equiv$. In **15** the $\Sigma_{C\text{-}Si\text{-}C}$ is 333.4, slightly lower than in **14**, and similar to values obtained for **11** – **13**. However, the Si-O distance in **15** at this level of theory is 1.83 Å, significantly longer than the Si–O bond in **14**. Similar to the example of ^{i}Pr$_3$Si–OTf (**10**) and [^{i}Pr$_3$Si][carborane], the longer Si–O bond distance in **15** results in the silylium-like character in this material.

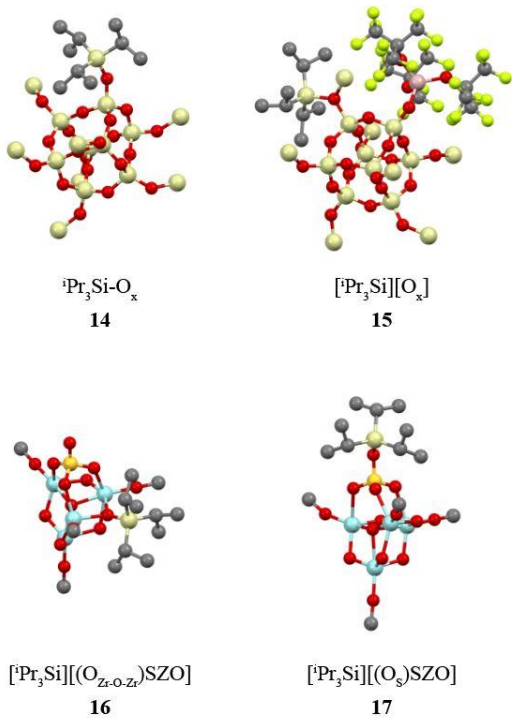

Figure 4. Calculated structures of **15 – 17** optimized at the Mo6-L/Zr, Br, I(SDD); 6-31G** level of theory. Hydrogens are omitted for clarity.

The **SZO** surface contains –OH sites that behave as strong acids and basic Zr–O–Zr bridges.[30] Experimental and computational studies show that surface bound organometallics interact with sulfates to form ion-pairs in well-defined heterogeneous catalysts,[31] which implies that ^{i}Pr$_3$Si–sites would interact with the sulfate as well. The **SZO** cluster model in Figure 4 is similar to those used previously in studies of sulfated oxides interacting with organometallics.[31e] In **16** the ^{i}Pr$_3$Si-site binds to a Zr–O–Zr bridge, and has an Si-O distance of 1.71 Å and $\Sigma_{C\text{-}Si\text{-}C}$ of 337.9°. In **17** the ^{i}Pr$_3$Si-site binds to the sulfate, and has a slightly longer Si-O distance of 1.77 Å and nearly identical $\Sigma_{C\text{-}Si\text{-}C}$ of 338.4°.

Table 2 contains calculated NMR data for **1** – **17** at the PBE/Si(TZ2P),DZ level of theory. In general, the calculated isotropic NMR chemical shifts are in good agreement with those obtained experimentally. Figure 5 contains these data graphically and shows that the calculated and experimental chemical shifts correlate well at this level of theory. In general, as the silicon in $R_3Si–X$ becomes closer to a free silylium the chemical shift value increases. The ^{i}Pr$_3$Si–X series illustrates this trend. Species that do not form silylium ions have chemical shift values < ~ 45 ppm. Free ^{i}Pr$_3$Si$^+$ is predicted to have a ^{29}Si NMR chemical shift of 343 ppm. [^{i}Pr$_3$Si][$CH_6B_{11}X_6$] have ^{29}Si NMR chemical shifts of ~100 ppm, between chemical shifts for free ^{i}Pr$_3$Si$^+$ and ^{i}Pr$_3$Si–X that do not form silylium ions.

Surface models follow similar trends. **14** does not capture structural trends consistent with a silylium ion, and has a calculated ^{29}Si NMR chemical shift of 15 ppm, close to experimental values for $R_3Si–O_X$ species reported previously.[15] However, **15** has a longer Si–O bond than **14**, and a calculated ^{29}Si

NMR chemical shift consistent with a "silylium-like" surface species.

Table 2. Calculated ^{29}Si NMR parameters of 1-17 at the PBE/Si,Zr(TZ2P), DZ level of theory.

R_3Si–X	δ_{calc}	δ_{expt}	Ω	σ_{11}	σ_{22}	σ_{33}	Ref
1	343	---	389	-157	-106	250	--
2	213	227[a]	279	32	33	311	- 6
3	94	93[a]	92	199	243	291	27
4	100	115[a]	87	208	232	276	2a
5	105	110[a]	103	188	221	291	2a
6	102	97[a]	113	197	217	299	2a
7	85	73[b]	136	170	285	307	8d
8	40	27[b]	145	217	318	362	8d
9	-54	-65[a]	42	368	398	410	8d
10	45	42[c]	22	283	293	305	32
11	42	36[d]	20	293	294	314	33
12	14	14[d]	36	310	317	346	34
13	-4	12[e]	52	310	360	360	35
14	15	~10[a]	30	310	320	340	15
15	64	70[a]	50	254	267	304	9b
16	27	-	28	305	310	332	-
17	42	55[a]	30	284	291	314	9a

[a] – solid-state measurement; [b] – recorded in *o*-dichlorobenzene; [c] – neat; [d] – recorded in $CDCl_3$; [e] – recorded in toluene-d_8

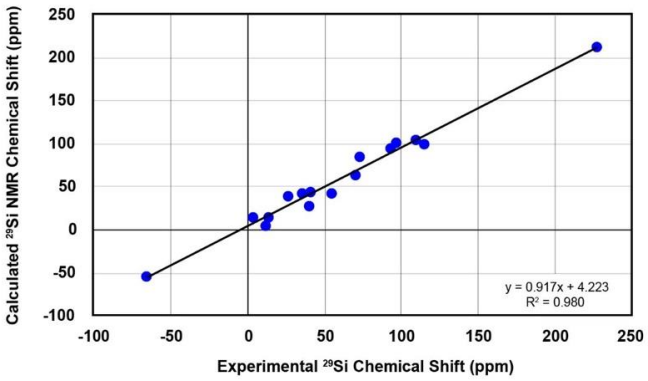

Figure 5. Plot of calculated and experimental isotropic ^{29}Si NMR chemical shift for **2** – **15** and **17**. The line is from linear regression analysis gives $R^2 = 0.980$.

Though this trend in ^{29}Si NMR chemical shift holds well for $^{i}Pr_3Si$–X, there are exceptions. For example, the ^{29}Si NMR chemical shift systematically decrease in the order $^{t}Bu_2SiH^+$ (85 ppm) > $^{t}BuSiH_2^+$ (40 ppm) > SiH_3^+ (-54 ppm), reproducing the experimental trends from ^{29}Si NMR measurements. $^{t}Bu_2SiH^+$, $^{t}BuSiH_2^+$ and SiH_3^+ are undoubtedly "silylium-like," but the latter two species have chemical shifts that appear inconsistent with this assignment. The origins of this trend will be discussed below.

Eq 1 shows that magnetic shielding is a 3 x 3 matrix, and eq 2 relates σ to more common δ scale used in NMR spectroscopy. The calculated values of σ_{ii} for **1** – **17** are given in Table 2. Table 2 also includes the span (Ω) of the shielding tensor, which is the difference of σ_{11} and σ_{33}. As X in $^{i}Pr_3Si$–X becomes more weakly coordinating Ω increases, indicating that the static powder pattern in the solid-state ^{29}Si NMR spectrum becomes broader. Figure 6 contains simulated static ^{29}Si NMR spectra for selected $^{i}Pr_3Si$–X. For example, $^{i}Pr_3Si$–OTf has a small Ω of 22 ppm and a narrow simulated static ^{29}Si NMR spectrum, Figure 6a. $Et_3Si(toluene)^+$ and $[^{i}Pr_3Si][CH_6B_{11}Br_6]$ have a larger Ω values than $^{i}Pr_3Si$–OTf and have broader simulated static ^{29}Si NMR spectrum (Figure 6b-c). The trend continues to the free silylium species; Mes_3Si^+ has a Ω of 279 ppm (Figure 6d), while free $^{i}Pr_3Si^+$ has the largest Ω of 389 ppm and is the broadest simulated spectrum (Figure 6e).

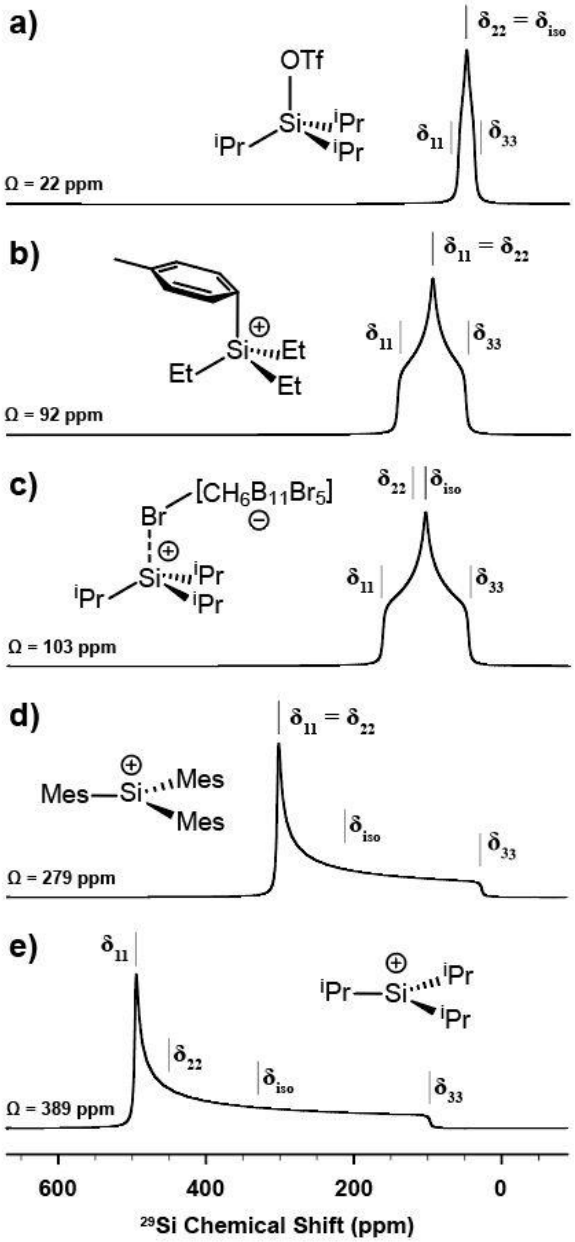

Figure 6. Static ^{29}Si solid-state NMR simulation of $^{i}Pr_3Si$–OTf (**10**), $Et_3Si(toluene)^+$ (**3**), $[^{i}Pr_3Si][CH_6B_{11}Br_6]$ (**5**), Mes_3Si^+ (**2**) and $^{i}Pr_3Si^+$ (**1**). Simulations of static were run using TopSpin 3.6.1 with 500 Hz line broadening using calculated NMR parameters from those shown in Table 2.

Eq 3 decomposes magnetic shielding into σ^d and σ^p. Figure 7 plots calculated σ_{tot}, σ^d and σ^p for σ_{11} in **1** – **17**. As the

calculated chemical shift increases σ decreases (black line), which is expected. The plot of σ^d (blue line) has a slope of 0, indicating that this term does not dramatically affect σ_{tot}, and therefore isotropic ^{29}Si NMR chemical shift, in **1** – **17**. However, σ^p clearly affects σ_{tot}, and is the main factor that results in the chemical shift trends observed in this series. The obvious implication from this result is that the arguments related to charge at silicon, which are a result of the σ^d term in eq 3, are not responsible for the downfield ^{29}Si NMR chemical shifts in R_3Si–X. The plots for σ_{22} and σ_{33} and their σ^p and σ^d contributions are provided in the Supplementary Information and follow this trend.

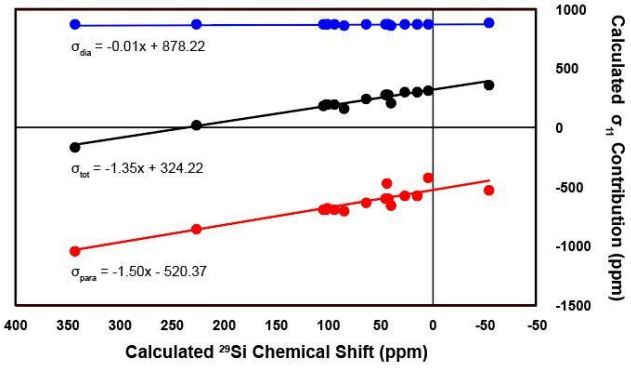

Figure 7. Comparison of calculated σ, σ^d and σ^p versus calculated isotropic ^{29}Si NMR chemical shift for σ_{11} in **1** – **17**.

As discussed above, eq 4 relates σ^p to coupling between occupied and unoccupied molecular orbitals through the angular momentum operator. This relationship is connected to the orientation of the magnetic shielding tensor. The orientations of the shielding tensors for **1** – **17** are remarkably similar, though the tensor surfaces vary across the series. The orientation of the shielding tensor and the tensor surface are shown for $^{i}Pr_3Si^+$ in Figure 8a and for $^{i}Pr_3Si$–Cl in Figure 8b as representative examples. The tensor orientation for both species roughly align with one another, with the most deshielded σ_{11} component and σ_{22} in or along the plane defined by the Si–C bonds and the most shielded σ_{33} perpendicular to this plane. $^{i}Pr_3Si^+$ has a highly anisotropic tensor surface, as expected for a formally sp^2 hybridized silicon. $^{i}Pr_3Si$–Cl has a nearly isotropic tensor surface, which is more typically observed for sp^3 hybridized silicon. This is correlated with the very large Ω for $^{i}Pr_3Si^+$ and the small Ω for $^{i}Pr_3Si$–Cl. Indeed, the tensor surface gradually transitions from the anisotropic surface for $^{i}Pr_3Si^+$ to the essentially isotropic surface for $^{i}Pr_3Si$–H across **1** – **17** (Figure S1).

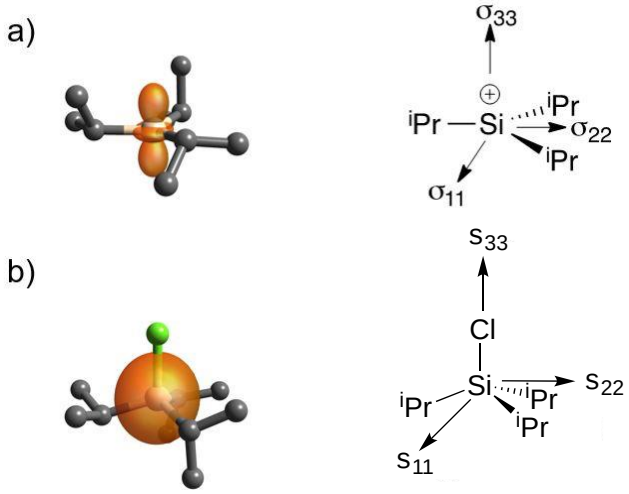

Figure 8. Shielding tensor surface plotted with TensorView 1.3[36] and shielding tensor orientation for $^{i}Pr3Si^+$ (a) and $^{i}Pr_3Si$-Cl (b).

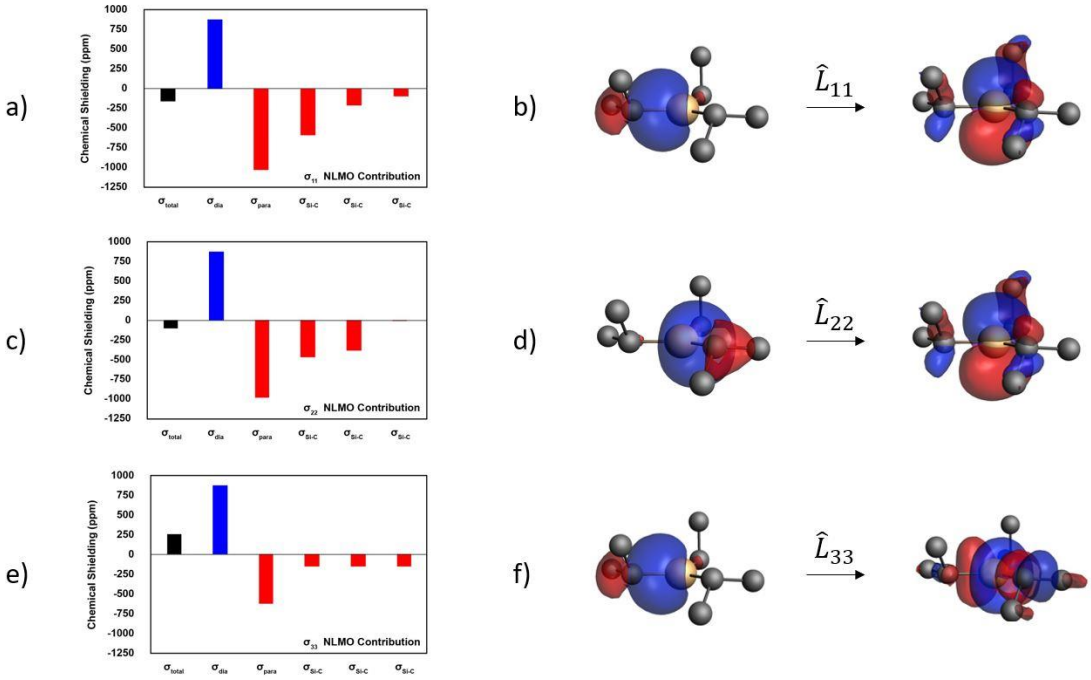

Figure 9. NLMO Contributions to σ_{11} (a), σ_{22} (c), and σ_{33} (e) and the major orbitals resulting in deshielding in $^{i}Pr_3Si^+$ (b, d, and f).

The orientation of the shielding tensor in for $^{i}Pr_3Si–X$ remain essentially constant across this series, suggesting that the σ^p contributions are of similar origin for a majority of the species in this study. A full natural localized molecular orbital (NLMO) description for the σ^p contributions to the shielding tensor of **1** are given in Figure 9. Figure 9a shows that the $\sigma_{Si\text{-}C}$ is the largest contributor to paramagnetic shielding in σ_{11}. Rotation of the $\sigma_{Si\text{-}C}$ NLMO by 90° about the σ_{11} axis results in the empty p-orbital on Si, the LUMO of $^{i}Pr_3Si^+$ (Figure 9b). The orientation of σ_{11}, and the contribution of a $\sigma_{Si\text{-}C}$ that is orthogonal to the LUMO in $^{i}Pr_3Si^+$, fulfills the prerequisites outlined above in eq 4 and Figure 2 for strong σ^p deshielding.

In $^{i}Pr_3Si^+$ σ_{22} is also in the plane defined by the three Si–C bonds, and roughly bisects the angle between one C–Si–C bond. This orientation couples two $\sigma_{Si\text{-}C}$ orbitals to the orthogonal empty p-orbital on silicon, which agrees with the NLMO decomposition of σ_{22} (Figure 9c-d). The diminished impact of σ_{33}, which is perpendicular to the plane defined by the Si–C bonds, on σ^p is also evident from Figure 9e–f. The major contributor to σ_{33} is also the Si–C bonds, but in this case the angular momentum operator couples the bonding $\sigma_{Si\text{-}C}$ orbital to higher energy $\sigma^*_{Si\text{-}C}$ orbitals.

A simplified MO diagram showing these transitions are given in Figure 10. This analysis explains why the Ω values for $R_3Si–X$ become larger as these species approach free R_3Si^+. The σ^p contributions to σ_{33} are small because of the large energy gap between $\sigma_{Si\text{-}C}$ and $\sigma^*_{Si\text{-}C}$ orbitals, which results in less deshielding of σ_{33} compared to σ_{11} and σ_{22}. This increases the difference between σ_{11} and σ_{33}, resulting in larger Ω values.

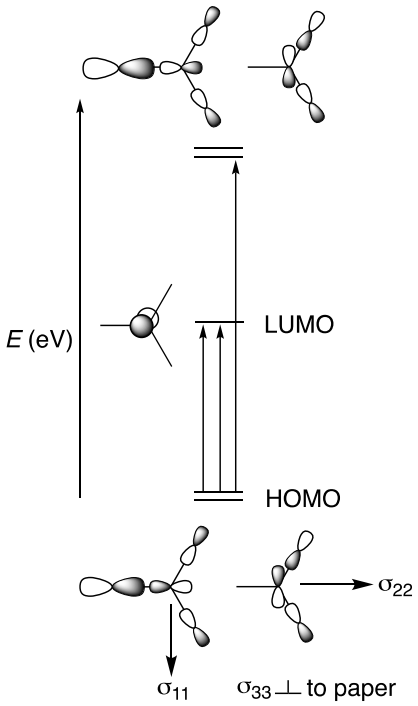

Figure 10. Simplified qualitative molecular orbital description of the orbitals coupled to σ^p through the angular momentum operator.

Approach of a weak nucleophile, such as toluene or a carborane anion, results in pyramidalization at silicon, and significantly less deshielded ^{29}Si NMR chemical shifts than predicted for $^{i}Pr_3Si^+$. The orientation of shielding tensor for the $^{i}Pr_3Si^+$ fragment in **5** is shown in Figure 11, and is oriented very similarly to the shielding tensor for **1**. NLMO decomposition shows that $\sigma_{Si\text{-}C}$ orbitals contribute to deshielding in σ_{11} and σ_{22}, indicating that these orbitals are also coupled to the p-orbital on silicon interacting with the halogen on the carborane anion, in this case a low-lying σ^* orbital. This result shows that the origin of ^{29}Si NMR deshielding is similar in **1** and **5**.

The difference in deshielding is not related to the difference in charge at silicon in **1** and **5**, but rather the pronounced increase in orbital energies involved in σ^p. Calculations of the canonical orbitals at this level of theory shows that the energy gap between the $\sigma_{Si\text{-}C}$ and the empty p-orbital on silicon in **1** is 3.61 eV, which is smaller than the energy gap between the $\sigma_{Si\text{-}C}$ and $\sigma^*_{Si\text{-}X}$ in **5** (5.57 eV, Figures S13-14).

As $^{i}Pr_3Si–X$ becomes increasingly pyramidal the σ_{11} becomes less deshielded, and the Ω decreases. For species that do not form silylium ions (**10** – **14**, **16**) the orientation of the shielding tensor is similar, though in this case the σ_{SiC} orbital couples to the $\sigma^*_{Si–X}$ orbital. NLMO decomposition of σ_{11}, and orbital rotations for **1** – **17** are given in the Supporting Information.

$[^{t}Bu_2SiH][CH_6B_{11}Br_6]$ (**7**), $[^{t}BuSiH_2][CH_6B_{11}Br_6]$ (**8**), and $[SiH_3][CH_6B_{11}Br_6]_2$ (**9**) seem to defy this trend. The orientation of shielding tensors for **5** and **7** – **9** are shown in Figure 11. The tensor plots of **5**, **7**, and **8** show similar anisotropies (Figure S1), which reflects their similar Ω values (Table 2, Entries 5, 7, and 8). At first glance the tensor orientations appear to have little in common. However, NLMO decomposition shows that in all three cases Si–C bonding orbitals are the major contributor to σ_{11}. In **5** and **8**, σ_{11} orients perpendicular to one Si–C bond, similar to $^{i}Pr_3Si^+$. However, σ_{11} in **7** orients along the Si–H bond. This alignment bisects the C–Si–C bond angle, and allows for efficient coupling of the Si–C bonding orbitals with the empty p-orbital on silicon through the angular momentum operator. These results show that the deshielding in σ_{11} in **7** and **8** is related to the other $R_3Si–X$.

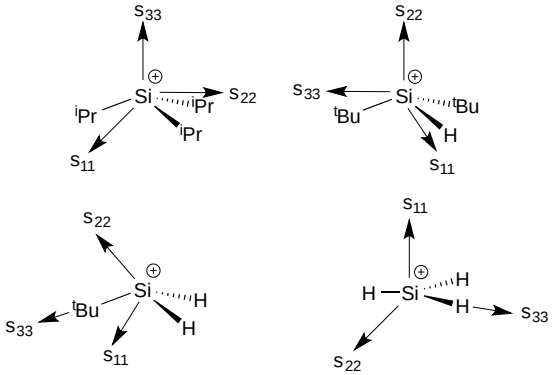

Figure 11. Orientation of the shielding tensors for **5**, **7** – **9**. The $[CH_6B_{11}Br_6]$ anions in **5**, **7** – **9** are omitted for clarity. **9** contains two $[CH_6B_{11}Br_6]$ anions.

The structural data in Table 1 relate $^{i}Pr_3Si^+$ to the SiH_3^+ fragment in **9**. Both contain planar silicon ($\Sigma_{R\text{-}Si\text{-}R}$ ~ 360°), suggesting that these two species should show similarly deshielded ^{29}Si NMR chemical shifts. However, these signals are predicted

to be separated by ~ 400 ppm, **9** being more shielded than $^{i}Pr_3Si^+$. In contrast to the tensor alignment in $^{i}Pr_3Si^+$, the shielding tensor of SiH_3^+ in **9** results in the σ_{11} component perpendicular to the plane defined by the three Si–H bonds. NLMO decomposition shows that the Si–H bonds are the major contributors to σ^p, which results in coupling between σ_{SiH} and σ^*_{SiH} through the angular momentum operator. This is unlike the other R_3Si^+ fragments studied here that couple σ_{SiR} orbitals to the the p-orbital on Si (Figure S7). This is a result of the two $[CH_6B_{11}Br_6]^-$ anions interacting with the p-orbital of the SiH_3^+ fragment in **9**, which results in a more shielded ^{29}Si NMR chemical shift than expected. This analysis also explains the small Ω value predicted for **9** in Table 2.

The net upfield ^{29}Si NMR chemical shift trend is in the order **2** > **7** > **8** >> **9**. Figure 12 shows the total σ^d and σ^p for each component of the shielding tensor. The σ^d is roughly constant in all four species, but σ^p gradually reduces in magnitude as Si–C bonds are replaced with Si–H bonds, which is likely a result of an increasing energy gap between the σ_{Si-C} and the σ^*_{Si-X} orbital in these species. The net effect of this reduction is a more shielded ^{29}Si NMR chemical shift value.

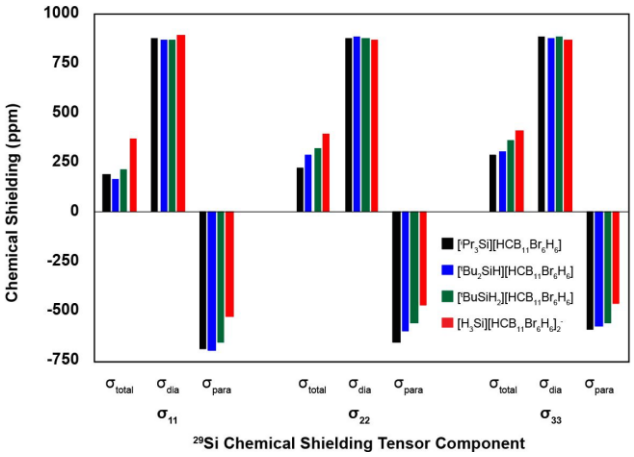

Figure 12. Total diamagnetic and paramagnetic shielding for each component of the shielding tensor in **5**, **7** – **9**.

Finally, plots of isotropic ^{29}Si NMR chemical shifts or Ω versus charge at this level of theory do not show an obvious correlation, Figure S12. This result is unambiguous, and indicates that charge does not relate to the NMR parameters discussed here.

Conclusion

DFT methods accurately reproduce the structural and ^{29}Si NMR chemical shift trends in a large family of molecular or surface R_3Si–X. Though these species span ~ 400 ppm on the ^{29}Si NMR chemical shift scale, analysis of the shielding tensor for these species shows remarkable similarities. In all cases except SiH_3^+, the most deshielded σ_{11} component of the shielding tensor orients to couple a Si–C bond with the empty p-orbital in silicon for silylium or "silylium-like" species, or couples a Si–C bond with the σ* Si–X orbital in species that do not form a silylium. This behavior is independent of the isotropic ^{29}Si NMR chemical shift value, and is not correlated with charge. SiH_3^+ has a unique shielding tensor orientation, which results in less σ^p than the other R_3Si–X species, and a significantly more shielded ^{29}Si NMR chemical shift.

What does ^{29}Si NMR reveal about the nature of a free silylium or "silylium-like" species? In many respects this question is related to the well-documented twists and turns of isolating and characterized R_3Si^+ species.[2a] While charge is not related to the isotropic ^{29}Si NMR chemical shift,[20] as R_3Si–X approaches R_3Si^+---X^- and ultimately R_3Si^+ the HOMO-LUMO gap decreases, resulting in an increase of σ^p and net deshielding of the ^{29}Si NMR chemical shift. However, increasing the s-character of the Si–R bonding orbital, as in $^{t}BuSiH_2^+$, results in larger energy gaps between the Si–H and empty p-orbital on silicon, which reduces σ^p contributions to shielding, and ultimately results in chemical shifts outside those expected for "silylium-like" species. These effects are more pronounced in SiH_3^+ because of a change in tensor orientation that results in less efficient coupling of orbitals through the angular momentum operator.

Based on structural parameters, the surface "silylium-like" models studied here show structural features in between those of $[^{i}Pr_3Si][CH_6B_{11}X_6]$ and $^{i}Pr_3Si$–X (X = OTf, Cl). However, the remarkably constant shielding tensor orientation in this series of R_3Si–X also relates to ^{29}Si NMR data for surface species. Similar to molecular R_3Si–X, oxides that contain –OH sites that behave as weakly coordination anions form "silylium-like" surface species. The σ_{11} deshielding is identical to that described for the molecular species. Given the wealth of $[R_3Si][WCA]$ salts synthetically accessible and the relative dearth of "silylium-like" surface species,[9] this information will be critical to analyze ^{29}Si NMR chemical shifts as new R_3Si^+ sites on surfaces become available.

ASSOCIATED CONTENT

Supporting Information

Calculated structures, shielding tensor plots, NLMO decomposition plots (pdf).
Coordinates for **1** – **17** (xyz).

The Supporting Information is available free of charge on the ACS Publications website.

AUTHOR INFORMATION

Corresponding Author

* matthew.conley@ucr.edu

Author Contributions

The manuscript was written through contributions of all authors

ACKNOWLEDGMENT

This study was supported by the National Science Foundation (CHE-1800561).

REFERENCES

(1) Olah, G. A.; Prakash, G. K. S.; Sommer, J.; Molnar, A.: *Superacid Chemistry*; John Wiley & sons, 2009.
(2) a) Reed, C. A. The Silylium Ion Problem, R3Si+. Bridging Organic and Inorganic Chemistry. *Acc. Chem. Res.* **1998**, *31*, 325-332; b) Reed, C. A. H+, CH3+, and R3Si+ Carborane Reagents: When Triflates Fail. *Acc. Chem. Res.* **2010**, *43*, 121-128.
(3) Reed, C. A.; Xie, Z.; Bau, R.; Benesi, A. Closely Approaching the Silylium Ion (R₃Si⁺). *Science* **1993**, *262*, 402-404.

(4) Lambert, J. B.; Zhang, S.; Stern, C. L.; Huffman, J. C. Crystal Structure of a Silyl Cation with No Coordination to Anion and Distant Coordination to Solvent. *Science* **1993**, *260*, 1917-1918.
(5) a)Pauling, L. Triethylsilyl Cations. *Science* **1994**, *263*, 983-983; b) Olah, G. A.; Rasul, G.; Li, X.-y.; Buchholz, H. A.; Sandford, G.; Prakash, G. K. S. Triethylsilyl Cations. *Science* **1994**, *263*, 983-984; c) Lambert, J. B.; Zhang, S. Response. *Science* **1994**, *263*, 984-985; d) Reed, C. A.; Xie, Z. Response. *Science* **1994**, *263*, 985-986.
(6)Kim, K.-C.; Reed, C. A.; Elliott, D. W.; Mueller, L. J.; Tham, F.; Lin, L.; Lambert, J. B. Crystallographic Evidence for a Free Silylium Ion. *Science* **2002**, *297*, 825-827.
(7) Xie, Z.; Manning, J.; Reed, R. W.; Mathur, R.; Boyd, P. D. W.; Benesi, A.; Reed, C. A. Approaching the Silylium (R3Si+) Ion: Trends with Hexahalo (Cl, Br, I) Carboranes as Counterions. *J. Am. Chem. Soc.* **1996**, *118*, 2922-2928.
(8) a) Ramírez-Contreras, R.; Bhuvanesh, N.; Zhou, J.; Ozerov, O. V. Synthesis of a Silylium Zwitterion. *Angew. Chem., Int. Ed.* **2013**, 52, 10313-10315; b) Wu, Q.; Roy, A.; Wang, G.; Irran, E.; Klare, H. F. T.; Oestreich, M. Synthesis of a Counteranion-Stabilized Bis(silylium) Ion. *Angew. Chem., Int. Ed.*; c) Wu, Q.; Qu, Z.-W.; Omann, L.; Irran, E.; Klare, H. F. T.; Oestreich, M. Cleavage of Unactivated Si–C(sp3) Bonds with Reed's Carborane Acids: Formation of Known and Unknown Silylium Ions. *Angew. Chem., Int. Ed.* **2018**, *57*, 9176-9179; d) Wu, Q.; Irran, E.; Müller, R.; Kaupp, M.; Klare, H. F. T.; Oestreich, M. Characterization of hydrogen-substituted silylium ions in the condensed phase. *Science* **2019**, *365*, 168-172; e) Küppers, T.; Bernhardt, E.; Eujen, R.; Willner, H.; Lehmann, C. W. [Me3Si][R-CB11F11]—Synthesis and Properties. *Angew. Chem., Int. Ed.* **2007**, *46*, 6346-6349.
(9) a)Culver, D. B.; Conley, M. P. Activation of C–F Bonds by Electrophilic Organosilicon Sites Supported on Sulfated Zirconia. *Angew. Chem., Int. Ed.* **2018**, *57*, 14902-14905; b) Culver, D. B.; Venkatesh, A.; Huynh, W.; Rossini, A. J.; Conley, M. P. Al(ORF)3 (RF = C(CF3)3) activated silica: a well-defined weakly coordinating surface anion. *Chem. Sci.* **2020**, *11*, 1510 - 1517.
(10) Widdifield, C. M.; Schurko, R. W. Understanding chemical shielding tensors using group theory, MO analysis, and modern density-functional theory. *Conc. Mag. Res. A* **2009**, *34A*, 91-123.
(11) West, R.; Buffy, J. J.; Haaf, M.; Müller, T.; Gehrhus, B.; Lappert, M. F.; Apeloig, Y. Chemical Shift Tensors and NICS Calculations for Stable Silylenes. *J. Am. Chem. Soc.* **1998**, *120*, 1639-1640.
(12) a) West, R.; Cavalieri, J. D.; Buffy, J. J.; Fry, C.; Zilm, K. W.; Duchamp, J. C.; Kira, M.; Iwamoto, T.; Müller, T.; Apeloig, Y. A Solid-State 1NMR and Theoretical Study of the Chemical Bonding in Disilenes. *J. Am. Chem. Soc.* **1997**, *119*, 4972-4976; b) Ichinohe, M.; Arai, Y.; Sekiguchi, A.; Takagi, N.; Nagase, S. A New Approach to the Synthesis of Unsymmetrical Disilenes and Germasilene: Unusual 29Si NMR Chemical Shifts and Regiospecific Methanol Addition. *Organometallics* **2001**, *20*, 4141-4143.
(13) Kravchenko, V.; Kinjo, R.; Sekiguchi, A.; Ichinohe, M.; West, R.; Balazs, Y. S.; Schmidt, A.; Karni, M.; Apeloig, Y. Solid-State 29Si NMR Study of RSiSiR: A Tool for Analyzing the Nature of the Si–Si Bond. *J. Am. Chem. Soc.* **2006**, *128*, 14472-14473.
(14) Buffy, J. J.; West, R.; Bendikov, M.; Apeloig, Y. Chemical Shielding Tensors for a Silicon–Carbon Double Bond. *J. Am. Chem. Soc.* **2001**, *123*, 978-979.
(15) Epping, J. D.; Yao, S.; Karni, M.; Apeloig, Y.; Driess, M. Si═X Multiple Bonding with Four-Coordinate Silicon? Insights into the Nature of the Si═O and Si═S Double Bonds in Stable Silanoic Esters and Related Thioesters: A Combined NMR Spectroscopic and Computational Study. *J. Am. Chem. Soc.* **2010**, *132*, 5443-5455.
(16) Auer, D.; Kaupp, M.; Strohmann, C. "Unexpected" 29Si NMR Chemical Shifts in Heteroatom-Substituted Silyllithium Compounds: A Quantum-Chemical Analysis. *Organometallics* **2004**, *23*, 3647-3655.
(17) Wiberg, K. B.; Hammer, J. D.; Zilm, K. W.; Cheeseman, J. R. NMR Chemical Shifts. 3. A Comparison of Acetylene, Allene, and the Higher Cumulenes. *J. Org. Chem.* **1999**, *64*, 6394-6400.
(18) Berger, S.; Fleischer, U.; Geletneky, C.; Lohrenz, J. C. W. The 13C Chemical Shift of the ipso Carbon Atom in Phenyllithium. *Chem. Ber.* **1995**, *128*, 1183-1186.
(19) a) Pinter, B.; Smith, K. T.; Kamitani, M.; Zolnhofer, E. M.; Tran, B. L.; Fortier, S.; Pink, M.; Wu, G.; Manor, B. C.; Meyer, K.; Baik, M.-H.; Mindiola, D. J. Cyclo-P3 Complexes of Vanadium: Redox Properties and Origin of the 31P NMR Chemical Shift. *J. Am. Chem. Soc.* **2015**, *137*, 15247-15261; b) Jochen, A.; Shaohui, Z. Analyzing Pt chemical shifts calculated from relativistic density functional theory using localized orbitals: The role of Pt 5d lone pairs. *Magn. Reson. Chem.* **2008**, *46*, S45-S55; c) Culver, D. B.; Huynh, W.; Tafazolian, H.; Ong, T.-C.; Conley, M. P. The β-Agostic Structure in (C5Me5)2Sc(CH2CH3): Solid-State NMR Studies of (C5Me5)2Sc–R (R=Me, Ph, Et). *Angew. Chem., Int. Ed.* **2018**, *57*, 9520-9523; d) Gordon, C. P.; Raynaud, C.; Andersen, R. A.; Copéret, C.; Eisenstein, O. Carbon-13 NMR Chemical Shift: A Descriptor for Electronic Structure and Reactivity of Organometallic Compounds. *Acc. Chem. Res.* **2019**, 52, 2278-2289; e) Wu, G.; Rovnyak, D.; Johnson, M. J. A.; Zanetti, N. C.; Musaev, D. G.; Morokuma, K.; Schrock, R. R.; Griffin, R. G.; Cummins, C. C. Unusual 31P Chemical Shielding Tensors in Terminal Phosphido Complexes Containing a Phosphorus–Metal Triple Bond. *J. Am. Chem. Soc.* **1996**, *118*, 10654-10655.
(20) Viesser, R. V.; Ducati, L. C.; Tormena, C. F.; Autschbach, J. The unexpected roles of σ and π orbitals in electron donor and acceptor group effects on the 13C NMR chemical shifts in substituted benzenes. *Chem. Sci.* **2017**, *8*, 6570-6576.
(21) M. J. Frisch, G. W. T., H. B. Schlegel, G. E. Scuseria, M. A. Robb, J. R. Cheeseman, G. Scalmani, V. Barone, G. A. Petersson, H. Nakatsuji, X. Li, M. Caricato, A. Marenich, J. Bloino, B. G. Janesko, R. Gomperts, B. Mennucci, H. P. Hratchian, J. V. Ortiz, A. F. Izmaylov, J. L. Sonnenberg, D. Williams-Young, F. Ding, F. Lipparini, F. Egidi, J. Goings, B. Peng, A. Petrone, T. Henderson, D. Ranasinghe, V. G. Zakrzewski, J. Gao, N. Rega, G. Zheng, W. Liang, M. Hada, M. Ehara, K. Toyota, R. Fukuda, J. Hasegawa, M. Ishida, T. Nakajima, Y. Honda, O. Kitao, H. Nakai, T. Vreven, K. Throssell, J. A. Montgomery Jr., J. E. Peralta, F. Ogliaro, M. Bearpark, J. J. Heyd, E. Brothers, K. N. Kudin, V. N. Staroverov, T. Keith, R. Kobayashi, J. Normand, K. Raghavachari, A. Rendell, J. C. Burant, S. S. Iyengar, J. Tomasi, M. Cossi, J. M. Millam, M. Klene, C. Adamo, R. Cammi, J. W. Ochterski, R. L. Martin, K. Morokuma, O. Farkas, J. B. Foresman and D. J. Fox. Gaussian 09. **2016**.
(22) Zhao, Y.; Truhlar, D. G. The M06 suite of density functionals for main group thermochemistry, thermochemical kinetics, noncovalent interactions, excited states, and transition elements: two new functionals and systematic testing of four M06-class functionals and 12 other functionals. *Theor. Chem. Acc.* **2008**, *120*, 215-241.
(23) te Velde, G.; Bickelhaupt, F. M.; Baerends, E. J.; Fonseca Guerra, C.; van Gisbergen, S. J. A.; Snijders, J. G.; Ziegler, T. Chemistry with ADF. *J. Comput. Chem.* **2001**, *22*, 931-967.
(24) Schreckenbach, G.; Ziegler, T. Calculation of NMR Shielding Tensors Using Gauge-Including Atomic Orbitals and Modern Density Functional Theory. *J. Phys. Chem.* **1995**, *99*, 606-611.
(25) Glendening, E. D.; Landis, C. R.; Weinhold, F. NBO 6.0: Natural bond orbital analysis program. *J. Comput. Chem.* **2013**, *34*, 1429-1437.
(26) Autschbach, J. Analyzing NMR shielding tensors calculated with two-component relativistic methods using spin-free localized molecular orbitals. *J. Chem. Phys.* **2008**, *128*, 164112.
(27) Lambert, J. B.; Zhang, S.; Ciro, S. M. Silyl Cations in the Solid and in Solution. *Organometallics* **1994**, *13*, 2430-2443.
(28) a) Conley, M. P.; Copéret, C.; Thieuleux, C. Mesostructured Hybrid Organic,ÄìSilica Materials: Ideal Supports for Well-Defined Heterogeneous Organometallic Catalysts. *ACS Catal.* **2014**, *4*, 1458-1469; b) Zapilko, C.; Widenmeyer, M.; Nagl, I.; Estler, F.; Anwander, R.; Raudaschl-Sieber, G.; Groeger, O.; Engelhardt, G. Advanced Surface Functionalization of Periodic Mesoporous Silica: Kinetic Control by Trisilazane Reagents. *J. Am. Chem. Soc.* **2006**, *128*, 16266-16276; c)Bluemel, J. Reactions of Ethoxysilanes with Silica: A Solid-State NMR Study. *J. Am. Chem. Soc.* **1995**, *117*, 2112-2113; d) Behringer, K. D.; Blümel, J. Reactions of Ethoxysilanes with Silica: A Solid-State NMR Study. *J. Liq. Chromatogr. Relat. Technol.* **1996**, *19*, 2753-2765.
(29)Del Rosal, I.; Gerber, I. C.; Poteau, R.; Maron, L. Grafting of Lanthanide Complexes on Silica Surfaces: A Theoretical Investigation. *J. Phys. Chem. A* **2010**, *114*, 6322-6330.

(30) Haase, F.; Sauer, J. The Surface Structure of Sulfated Zirconia Periodic ab Initio Study of Sulfuric Acid Adsorbed on ZrO2(101) and ZrO2(001). *J. Am. Chem. Soc.* **1998**, *120*, 13503-13512.
(31) a) Kaphan, D. M.; Klet, R. C.; Perras, F. A.; Pruski, M.; Yang, C.; Kropf, A. J.; Delferro, M. Surface Organometallic Chemistry of Supported Iridium(III) as a Probe for Organotransition Metal–Support Interactions in C–H Activation. *ACS Catal.* **2018**, *8*, 5363-5373; b) Marie, S. M.; P., N. C.; Alak, B.; Alessandro, M.; Massimiliano, D.; J., M. T. Single-Face/All-cis Arene Hydrogenation by a Supported Single-Site do Organozirconium Catalyst. *Angew. Chem., Int. Ed.* **2016**, 55, 5263-5267; c) Stalzer, M.; Delferro, M.; Marks, T. Supported Single-Site Organometallic Catalysts for the Synthesis of High-Performance Polyolefins. *Catal. Lett.* **2015**, *145*, 3-14; d) Klet, R. C.; Kaphan, D. M.; Liu, C.; Yang, C.; Kropf, A. J.; Perras, F. A.; Pruski, M.; Hock, A. S.; Delferro, M. Evidence for Redox Mechanisms in Organometallic Chemisorption and Reactivity on Sulfated Metal Oxides. *J. Am. Chem. Soc.* **2018**, *140*, 6308-6316; e) Syed, Z. H.; Kaphan, D. M.; Perras, F. A.; Pruski, M.; Ferrandon, M. S.; Wegener, E. C.; Celik, G.; Wen, J.; Liu, C.; Dogan, F.; Goldberg, K. I.; Delferro, M. Electrophilic Organoiridium(III) Pincer Complexes on Sulfated Zirconia for Hydrocarbon Activation and Functionalization. *J. Am. Chem. Soc.* **2019**, *141*, 6325-6337; f) Williams, L. A.; Guo, N.; Motta, A.; Delferro, M.; Fragala, I. L.; Miller, J. T.; Marks, T. J. Surface structural-chemical characterization of a single-site do heterogeneous arene hydrogenation catalyst having 100% active sites. *Proc. Nat. Acad. Sci. USA* **2013**, *110*, 413-418; g) Rodriguez, J.; Culver, D. B.; Conley, M. P. Generation of Phosphonium Sites on Sulfated Zirconium Oxide: Relationship to Brønsted Acid Strength of Surface –OH Sites. *J. Am. Chem. Soc.* **2019**, *141*, 1484-1488; h) Culver, D. B.; Tafazolian, H.; Conley, M. P. A Bulky Pd(II) α-Diimine Catalyst Supported on Sulfated Zirconia for the Polymerization of Ethylene and Copolymerization of Ethylene and Methyl Acrylate. *Organometallics* **2018**, *37*, 1001-1006; i) Tafazolian, H.; Culver, D. B.; Conley, M. P. A Well-Defined Ni(II) α-Diimine Catalyst Supported on Sulfated Zirconia for Polymerization Catalysis. *Organometallics* **2017**, *36*, 2385-2388.
(32) Olah, G. A.; Laali, K.; Farooq, O. Organometallic chemistry. 21. Silyl trifluoromethanesulfonate (triflate)-boron trichloride (tribromide) complexes. *Organometallics* **1984**, *3*, 1337-1340.
(33) Zhang, C.; Patschinski, P.; Stephenson, D. S.; Panisch, R.; Wender, J. H.; Holthausen, M. C.; Zipse, H. The calculation of 29Si NMR chemical shifts of tetracoordinated silicon compounds in the gas phase and in solution. *Phys. Chem. Chem. Phys.* **2014**, *16*, 16642-16650.
(34) Savela, R.; Zawartka, W.; Leino, R. Iron-Catalyzed Chlorination of Silanes. *Organometallics* **2012**, *31*, 3199-3206.
(35) Xie, Z.; Liston, D. J.; Jelínek, T.; Mitro, V.; Bau, R.; Reed, C. A. A new weakly coordinating anion: approaching the silylium (silicenium) ion. *Chem. Commun.* **1993**, 384-386.
(36) Young, R. P.; Lewis, C. R.; Yang, C.; Wang, L.; Harper, J. K.; Mueller, L. J. TensorView: A software tool for displaying NMR tensors. *Magn. Reson. Chem.* **2019**, *57*, 211-223.

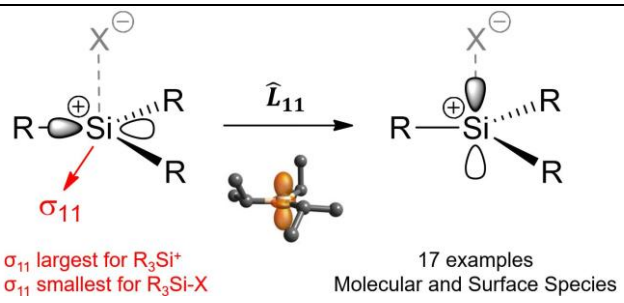

- σ_{11} largest for R_3Si^+
- σ_{11} smallest for R_3Si-X

17 examples
Molecular and Surface Species